XRF Core Scanning

Site 1258

XRF Core Scanner data for ODP Site 1258 were measured from 134.61 to 212.49 rmcd. XRF Core Scanner data were collected every 2 cm down-core over a 1 cm^2 area with a slit size of 10 mm using a generator setting of 20 kV, 0.087 mA and a sampling time of 20 seconds directly at the split core surface of the archive half. The data reported here have been acquired by XRF Core Scanner I at MARUM using a KEVEX Psi Peltier Cooled Silicon Detector and a KEVEX X-ray Tube 52500008-02 with the target material molybdenum (Mo). This is the same setting as used in Westerhold and Röhl (2009). Data are provided in table S1.

Site 1262

XRF Core Scanner data for ODP Site 1262 were measured with XRF Core Scanner I at the MARUM-University of Bremen. XRF Core Scanner data were collected every 2 cm down-core over a 1 cm^2 area with a slit size of 10 mm using a generator setting of 20 kV, 0.087 mA and a sampling time of 20 seconds directly at the split core surface of the archive half. Data are provided in Table S2.

To intercalibrate Fe intensity data obtained from different generations of XRF core scanners and their distinct hardware settings, we scanned an intervals covering the full range of Fe intensities at 1262. Linear regression of the Fe intensity data (Fig. S3) provides the following formula to calibrate Fe data from XRF I to XRF II as published in Westerhold et al. (2007):

Fe Area XRF I = 1.7709* Fe Area XRF I

After the intercalibration data from XRF I and II runs have been combined as in supplementary table S2. Data used for the calibration are given in supplementary table S3.

Site 1263

X-ray fluorescence (XRF) core scanning data for ODP Site 1263 were collected with XRF Core Scanner II at the MARUM-University of Bremen. Due to revision of the shipboard splice (Westerhold et al., 2015) XRF data reported here have been obtained in two runs separated by 4 years. Sections 1263B9 1-4, 1263A15 4-5, 1263B10 3-5,

1263A16 2 60-150cm, 1263A16 3-6, were measured in 2004 every 2 cm down-core over a 1 cm^2 area using a generator setting of 20 kV, 0.05 mA, and a sampling time of 30 seconds. XRF Scanner II in 2004 was operated with a AMPTEK Inc. XR-100CR detector with 173eV X-ray resolution, the PX2T/CR Amplifier from AMPTEK Inc. and an Oxford Instruments 50W XTF5011 X-ray tube with rhodium (Rh) target. Sections 1263B12H2 22-148cm, 1263B12H6 2-100cm, 1263A19H2 76 to A19H 148cm, 1263B14H1 70 to B14H2 58cm, were measured in 2008 every 2 cm down-core over a 1 cm^2 area using a generator setting of 10 kV, 0.35 mA, and a sampling time of 20 seconds . XRF Scanner II in 2008 was operated with a X-PIPS detector from Canberra Industries Model SXP 5C-200-1500 V3 with 192eV X-ray resolution, the Canberra Digital Spectrum Analyzer DAS 1000 and an Oxford Instruments 50W XTF5011 X-ray tube 93057 with rhodium (Rh) target material.

To compensate for the different XRF score scanner settings of the first and second run several intervals covering the full range of Fe intensities at 1263 have been scanned during both acquisition campaigns. Linear regression of the Fe intensity data from both runs provide the following formula to calibrate Fe data from the second run to the first:

Fe Area FirstRun = (0.5831* Fe Area SecondRun) - 577.58

After calibration the data from both runs have been combined as in supplementary table S4. Data used for the calibration are given in Westerhold et al. (subm. Geology).

Site 1265

X-ray fluorescence (XRF) core scanning data for ODP Site 1265 were collected with XRF Core Scanner II at the MARUM-University of Bremen. Data were collected in 2004 every 2 cm down-core over a 1 cm^2 area using a generator setting of 20 kV, 0.05 mA, and a sampling time of 30 seconds. This is the same setting as used in Westerhold et al., (2007). Data are provided in Table S5.

Site 1267

X-ray fluorescence (XRF) core scanning data measured in 2004 for ODP Site 1267 were collected with XRF Core Scanner II at the MARUM-University of Bremen every 1-2 cm down-core over a 1 cm^2 area using a generator setting of 20 kV, 0.05 mA, and a sampling time of 30 seconds. This is the same setting as used in Westerhold et al., (2008).

Data collected in 2012 were obtained every 2 cm down-core over a 1 cm^2 area with a down-core slit size of 12 mm using generator settings of 10 kV, a current of 0.150 mA, and a sampling time of 20 seconds directly at the split core surface of the archive half with XRF Core Scanner III (AVAATECH Serial No. 12) at the MARUM - University of Bremen. The data reported here have been acquired by a Canberra X-PIPS Silicon Drift Detector (SDD; Model SXD 15C-150-500) with 150eV X-ray resolution, the Canberra Digital Spectrum Analyzer DAS 1000 and an Oxford Instruments 100W Neptune X-ray tube with rhodium (Rh) target material.

To compensate for the different XRF score scanner settings of the runs in 2004 and 2012 on sediments from Site 1267 two core sections were run during both acquisition campaigns. Linear regression of the Fe intensity data from both runs provide the following formula to calibrate Fe data from the 2004 run to the 2012 run:

XRF3 Fe Area 2012 = 6.9077* XRF2 Fe Area 2004

After calibration the data from both runs have been combined as in supplementary table S6. Data used for the calibration are given in Table S7.

Raw data spectra obtained with XRF II and III were processed by the Analysis of X-ray spectra using the Iterative Least square software (WIN AXIL) package from Canberra Eurisys. The split core surfaces of all cores were covered with a 4 mm thin SPEXCerti Prep Ultralene foil to avoid contamination of the XRF measurement unit and desiccation of the sediment.

References:

Agnini, C., Fornaciari, E., Raffi, I., Rio, D., Röhl, U., and Westerhold, T.: High-resolution nannofossil biochronology of middle Paleocene to early Eocene at ODP Site 1262: Implications for calcareous nannoplankton evolution, Marine Micropaleontology, 64, 215-248, 10.1016/j.marmicro.2007.05.003, 2007.

Bowles, J.: Data report: Revised magnetostratigraphy and magnetic mineralogy of sediments from Walvis Ridge, Leg 208, in: Proc. ODP, Sci. Results, 208: College Station, TX (Ocean Drilling Program), edited by: Kroon, D., Zachos, J. C., and Richter, C., 10.2973/odp.proc.sr.114.156.1991, 2006.

Cande, S. C., and Kent, D. V.: A New Geomagnetic Polarity Time Scale for the late Cretaceous and Cenozoic, Journal of Geophysical Research, 97, 13,917-913,951, 1992.

Cande, S. C., and Kent, D. V.: Revised calibration of the geomagnetic polarity timescale for the Late Cretaceous and Cenozoic, Journal of Geophysical Research, 100, 6093-6095, 1995.

Kirtland Turner, S., Sexton, P. F., Charles, C. D., and Norris, R. D.: Persistence of carbon release events through the peak of early Eocene global warmth, Nature Geosci, 7, 10.1038/ngeo2240, 2014.

Laskar, J., Fienga, A., Gastineau, M., and Manche, H.: La2010: a new orbital solution for the long-term motion of the Earth, Astronomy and Astrophysics, 532, 15, 10.1051/0004-6361/201116836, 2011.

Lauretano, V., Littler, K., Polling, M., Zachos, J. C., and Lourens, L. J.: Frequency, magnitude and character of hyperthermal events at the onset of the Early Eocene Climatic Optimum, Clim. Past, 11, 1313-1324, 10.5194/cp-11-1313-2015, 2015.

Lauretano, V., Hilgen, F. J., Zachos, J. C., and Lourens, L. J.: Astronomically tuned age model for the early Eocene carbon isotope events: A new high-resolution δ13Cbenthic record of ODP Site 1263 between ~49 and ~54 Ma, Newsletters on Stratigraphy, 49, 383–400, 10.1127/nos/2016/0077, 2016.

Littler, K., Röhl, U., Westerhold, T., and Zachos, J. C.: A high-resolution benthic stable-isotope record for the South Atlantic: Implications for orbital-scale changes in Late Paleocene–Early Eocene climate and carbon cycling, Earth and Planetary Science Letters, 401, 18-30, 10.1016/j.epsl.2014.05.054, 2014.

Lourens, L. J., Sluijs, A., Kroon, D., Zachos, J. C., Thomas, E., Röhl, U., Bowles, J., and Raffi, I.: Astronomical pacing of late Palaeocene to early Eocene global warming events, Nature, 435, 1083-1087, 10.1038/nature03814, 2005.

Lurcock, P. C. and Wilson, G. S.: PuffinPlot: A versatile, user- friendly program for paleomagnetic analysis, Geochem. Geo- phys. Geosys., 13, Q06Z45, doi:10.1029/2012GC004098, 2012.

McCarren, H., Thomas, E., Hasegawa, T., Röhl, U., and Zachos, J. C.: Depth dependency of the Paleocene-Eocene carbon isotope excursion: Paired benthic and terrestrial biomarker records (Ocean Drilling Program Leg 208, Walvis Ridge), Geochemistry, Geophysics, Geosystems, 9, 10.1029/2008GC002116, 2008.

Röhl, U., Westerhold, T., Bralower, T. J., and Zachos, J. C.: On the duration of the Paleocene-Eocene thermal maximum (PETM), Geochemistry, Geophysics, Geosystems, 8, 10.1029/2007GC001784, 2007.

Sexton, P. F., Norris, R. D., Wilson, P. A., Pälike, H., Westerhold, T., Röhl, U., Bolton, C. T., and Gibbs, S.: Eocene global warming events driven by ventilation of oceanic dissolved organic carbon, Nature, 471, 349-352, 10.1038/nature09826, 2011.

Stap, L., Sluijs, A., Thomas, E., and Lourens, L.: Patterns and magnitude of deep sea carbonate dissolution during Eocene Thermal Maximum 2 and H2, Walvis Ridge, southeastern Atlantic Ocean, Paleoceanography, 24, 10.1029/2008PA001655, 2009.

Stap, L., Lourens, L. J., Thomas, E., Sluijs, A., Bohaty, S., and Zachos, J. C.: High-resolution deep-sea carbon and oxygen isotope records of Eocene Thermal Maximum 2 and H2, Geology, 38, 607-610, 10.1130/g30777.1, 2010.

Suganuma, Y., and Ogg, J. G.: Campanian through Eocene magnetostratigraphy of Sites 1257–1261, ODP Leg 207, Demerara Rise (western equatorial Atlantic), in: Proc. ODP, Sci. Results, 207: College Station, TX (Ocean Drilling Program), edited by: Mosher, D. C., Erbacher, J., and Malone, M. J., 1-48, 10.2973/odp.proc.sr.207.102.2006, 2006.

Westerhold, T., Röhl, U., Laskar, J., Bowles, J., Raffi, I., Lourens, L. J., and Zachos, J. C.: On the duration of magnetochrons C24r and C25n and the timing of early Eocene global warming events: Implications from the Ocean Drilling Program Leg 208 Walvis Ridge depth transect, Paleoceanography, 22, 10.1029/2006PA001322, 2007.

Westerhold, T., Röhl, U., Raffi, I., Fornaciari, E., Monechi, S., Reale, V., Bowles, J., and Evans, H. F.: Astronomical calibration of the Paleocene time, Palaeogeography, Palaeoclimatology, Palaeoecology, 257, 377-403, 10.1016/j.palaeo.2007.09.016, 2008.

Westerhold, T., and Röhl, U.: High resolution cyclostratigraphy of the early Eocene - new insights into the origin of the Cenozoic cooling trend, Clim Past, 5, 309-327, 10.5194/cp-5-309-2009, 2009.

Westerhold, T., Röhl, U., and Laskar, J.: Time scale controversy: Accurate orbital calibration of the early Paleogene, Geochem. Geophys. Geosyst., 13, Q06015, 10.1029/2012gc004096, 2012.

Westerhold, T., Röhl, U., Frederichs, T., Bohaty, S. M., and Zachos, J. C.: Astronomical calibration of the geological timescale: closing the middle Eocene gap, Clim. Past Discuss., 11, 1665-1699, 10.5194/cpd-11-1665-2015, 2015a.

Westerhold, T., Röhl, U., Frederichs, T., Bohaty, S. M., and Zachos, J. C.: Astronomical calibration of the geological timescale: closing the middle Eocene gap, Clim. Past, 11, 1181-1195, 10.5194/cp-11-1181-2015, 2015b.

Zachos, J. C., Röhl, U., Schellenberg, S. A., Sluijs, A., Hodell, D. A., Kelly, D. C., Thomas, E., Nicolo, M., Raffi, I., Lourens, L. J., McCarren, H., and Kroon, D.: Rapid Acidification of the Ocean During the Paleocene-Eocene Thermal Maximum, Science, 308, 1611-1615, 10.1126/science.1109004, 2005.

Zachos, J. C., McCarren, H., Murphy, B., Röhl, U., and Westerhold, T.: Tempo and scale of late Paleocene and early Eocene carbon isotope cycles: Implications for the origin of hyperthermals, Earth and Planetary Science Letters, 299, 242-249, 10.1016/j.epsl.2010.09.004, 2010.

Figure Caption

Figure S1 a-c. Overview of geochemical, magneto- and biostratigraphic data from Leg 208 sites 1262, 1263, 1265 and 1267 plotted on their composite depth scales spanning Chron C21n to C24r.

Figure S2. Overview of geochemical, magneto- and biostratigraphic data from Site 1258 plotted on the composite depth spanning Chron C21n to C24r.

Figure S3. Intercalibration for Fe intensity data obtained from different generations of XRF core scanners and their distinct hardware.

Figure S4 a-b. Overview of characteristic remanent magnetization results and data from Leg 208 Sites 1262, 1263, 1265 and 1267 versus depth.

Figure S5. Showcase Zijderveld plots (Z plots) for samples from C22n, C22r and C22n/C22r.

Figure S6. Correlation between ODP Site 1263 and 1265 reveals a gap of three sedimentary cycles in 1263.

Figure S7. Overview of bio- and magnetostratigraphic data, XRF core scanning Fe intensity data and core images from ODP Site 1258, 1262, 1263, 1265 and 1267 from 300-340 revised meters composite depth of Site 1263.

Figure S8. Correlation of bulk carbon isotope data Site 1265 and benthic carbon isotope data Site 1258 to show the missing or condensed interval in Leg 208 sedimentary sequence.

Figure S9. Plot to illustrate the detrending procedure applied to the bulk and benthic stable carbon isotope data compilations.

Figure S10. Evolutive wavelet spectra for XRF Fe (1263, 1267) and carbon isotope records versus depth to identify orbital cycles.

Figure S11. Time series analysis to identify the 100-kyr and 405-kyr eccentricity components in XRF Fe intensity and carbon isotope data.

Figure S12. 405-kyr tuning of the benthic carbon isotope compilation to La2010b/c from 47.5-56 Ma.

Figure S13. Sedimentation rates for Site 1258 and 1263 applying different age models versus depth and magnetostratigraphy in the interval from Chron C22r to C24n.1n.

Figure S14. Effect of the 2 and 3 cycle 405-kyr model of Lauretano et al. (2016) (**A**) and the new 405-kyr cycle model developed in this study (**B**) on ODP Site 1258 XRF Fe intensity data and the benthic carbon isotope compilation.

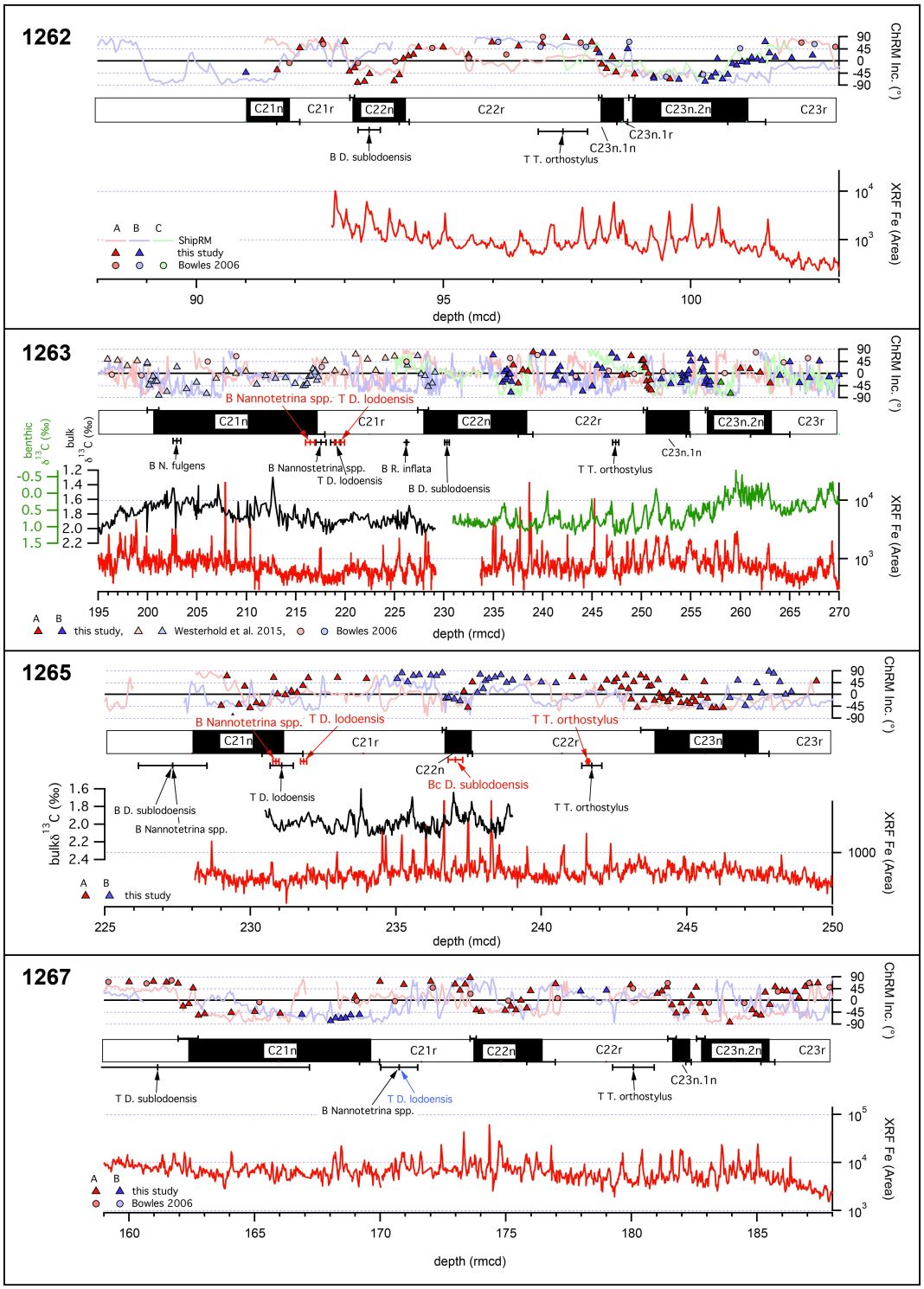

Figure S1a. Overview of geochemical, magneto- and biostratigraphic data from Leg 208 sites 1262, 1263, 1265 and 1267 plotted on their composite depth scales spanning Chron C21n to C23r. XRF core scanning Fe intensity data (red), bulk (black) and benthic (green) stable isotope data, shipboard u-channel (light red, blue and green) and shorebased discrete sample inclination data from characteristic remanent magnetization analysis (filled symbols with lighter colors from published records and full colors from this study), magnetostratigraphic interpretation and calcareous nannofossil events (black, blue – published; red – this study).

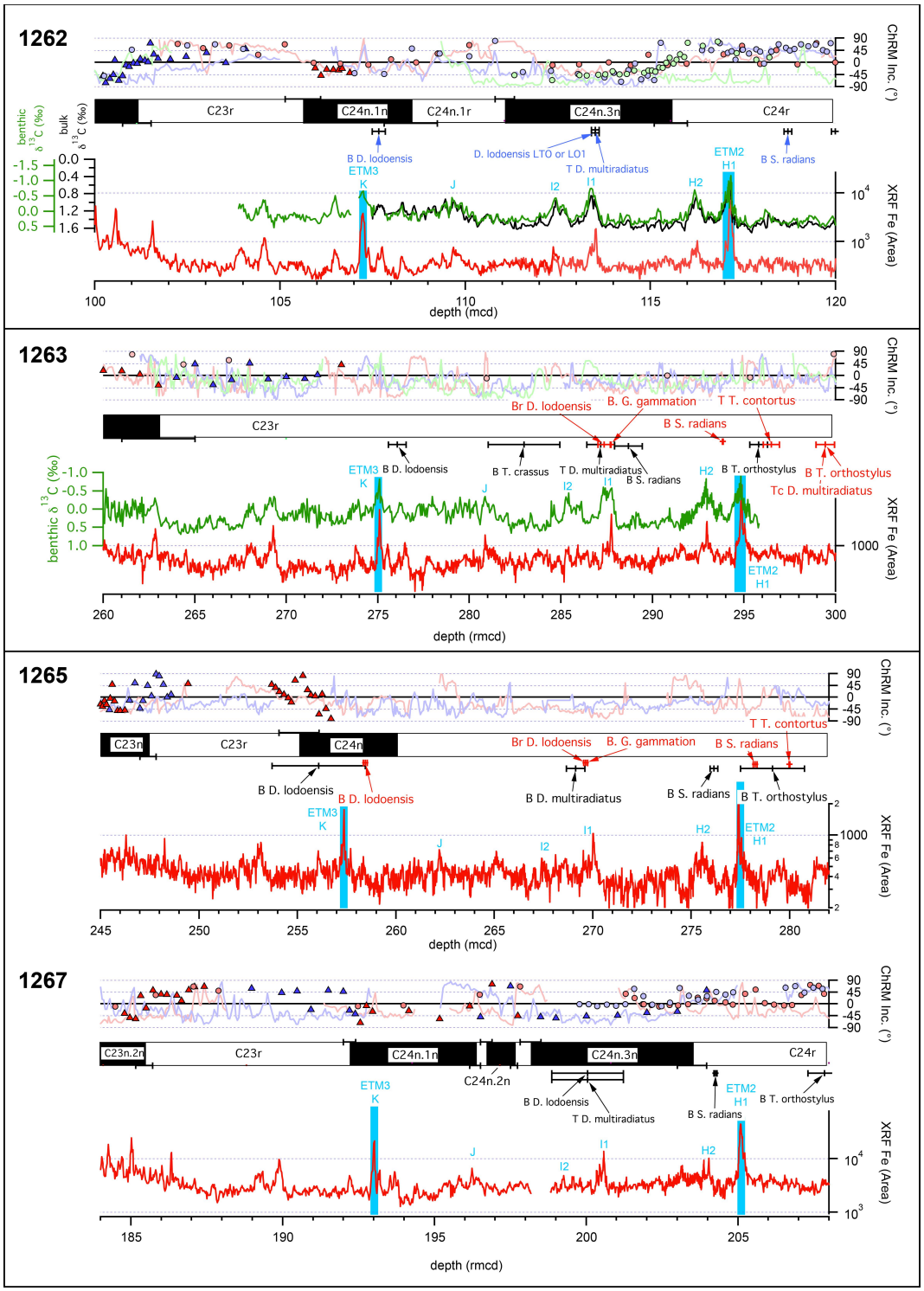

Figure S1b. Overview of geochemical, magneto- and biostratigraphic data from Leg 208 sites 1262, 1263, 1265 and 1267 plotted on their composite depth scales spanning Chron C23r to C24r / ETM2. For legend see Fig. S1a text. Eocene hyperthermal events ETM2 and ETM3 are highlighted.

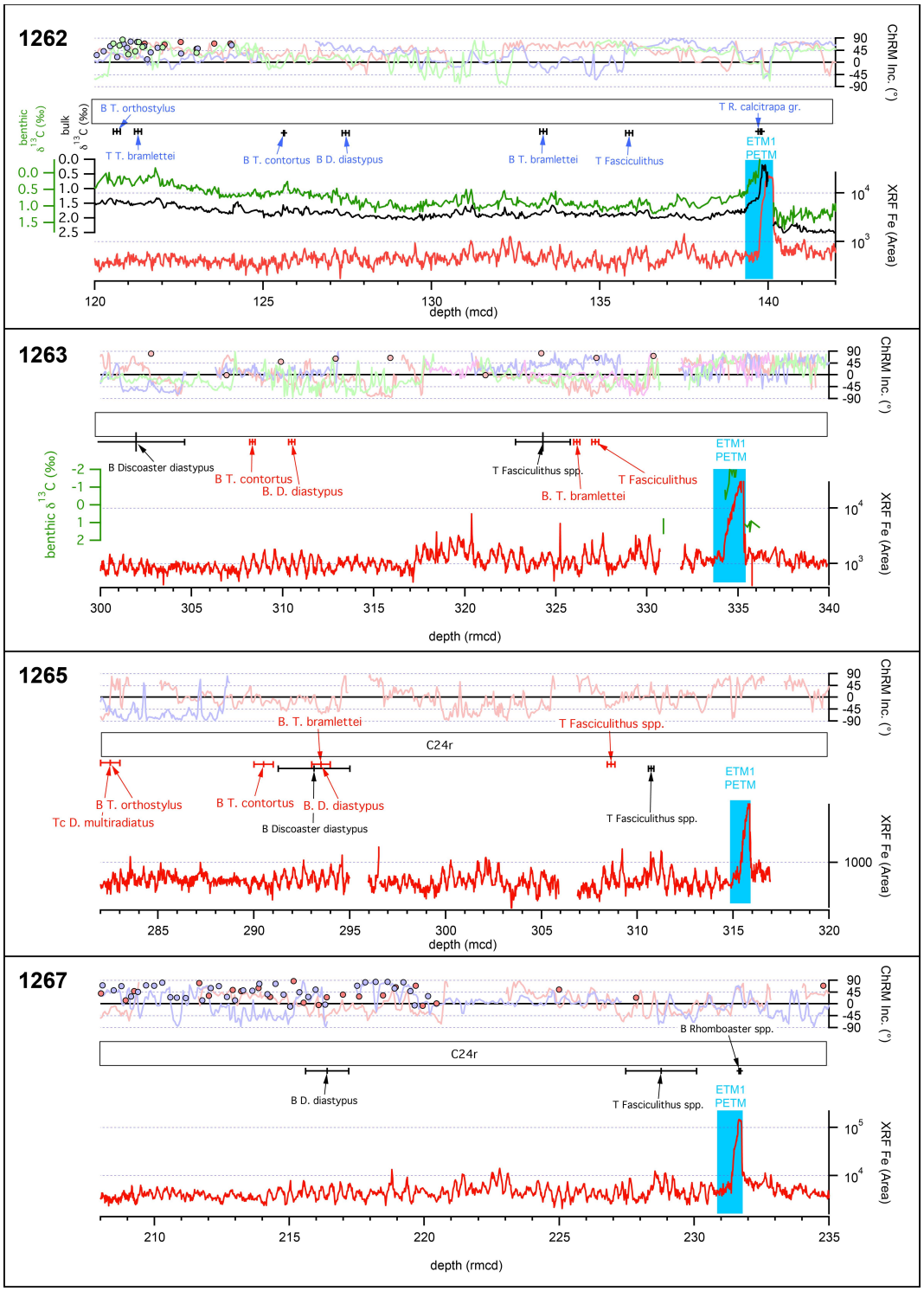

Figure S1c. Overview of geochemical, magneto- and biostratigraphic data from Leg 208 sites 1262, 1263, 1265 and 1267 plotted on their composite depth scales spanning Chron C24r after the PETM (ETM1). For legend see Fig. S1a text.

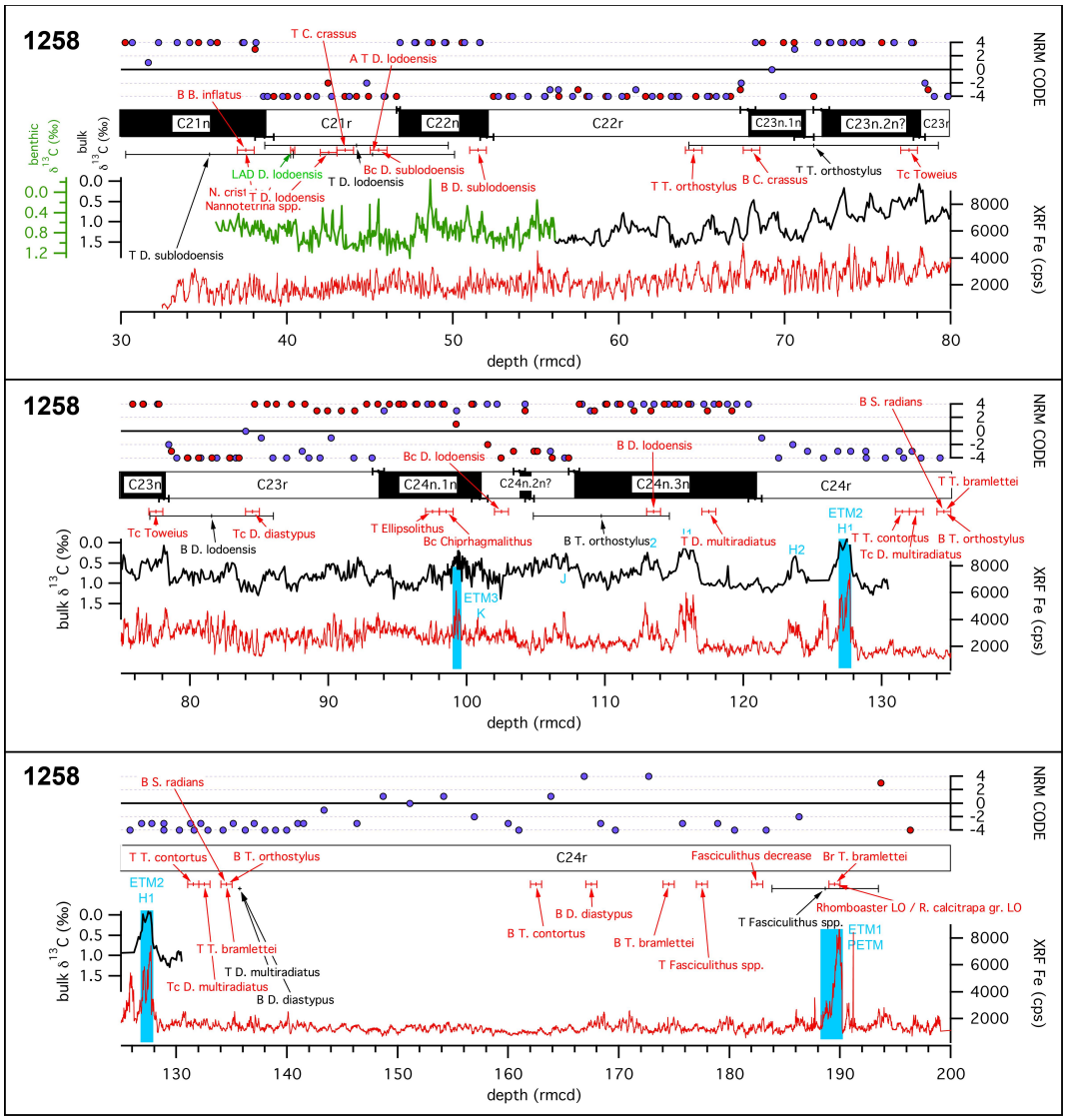

Figure S2. Overview of geochemical, magneto- and biostratigraphic data Site 1258 plotted on composite depth spanning Chron C21n to C24r after the PETM (ETM1). XRF core scanning Fe intensity data (red), bulk (black) and benthic (green) stable isotope data, shorebased discrete sample inclination results of natural remanent magnetization analysis (Suganuma and Ogg, 2006), magnetostratigraphic interpretation and calcareous nannofossil events (black - shipboard, green – other published; red – this study).

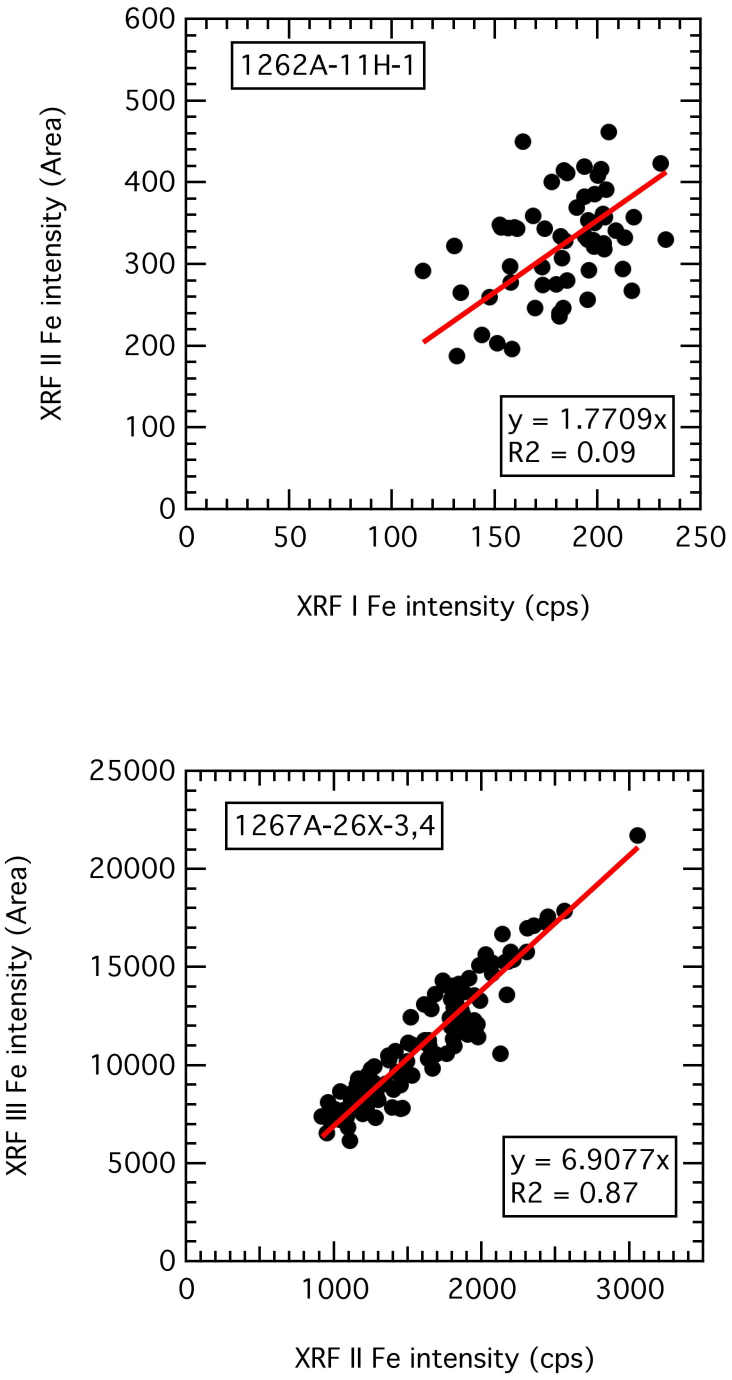

Figure S3 Intercalibration for Fe intensity data obtained from different generations of XRF core scanners and their distinct hardware. Upper panel shows intercalibration for Site 1262 XRF Fe intensity data obtained by MARUM XRF I and MARUM XRF II. Lower shows intercalibration for Site 1267 XRF Fe intensity data obtained by MARUM XRF II and MARUM XRF III. See supplementary text for details.

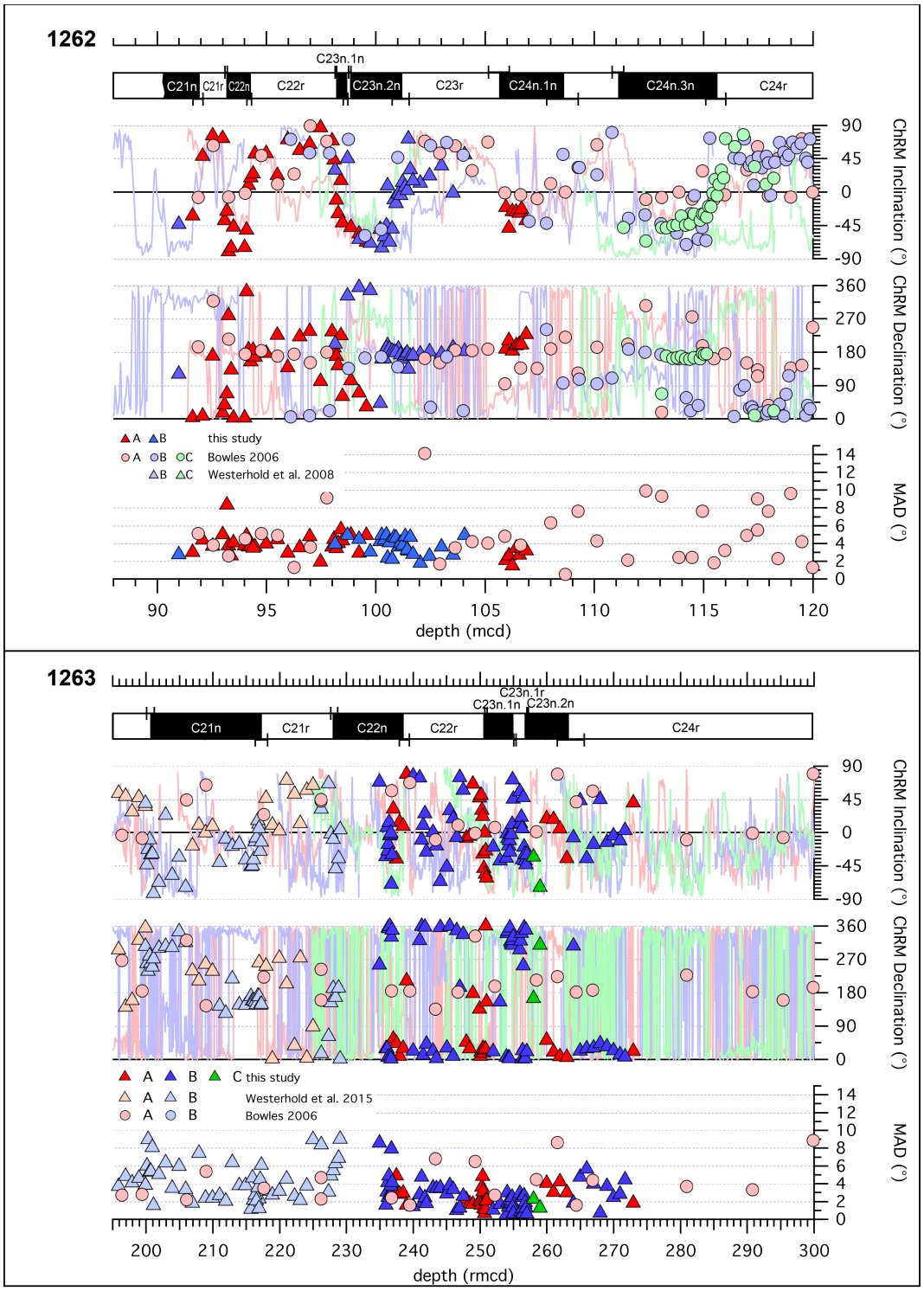

Figure S4a Overview of characteristic remanent magnetization results and data from Leg 208 Sites 1262 and 1263 versus depth. Given for each Site are the maximum angular deviation (MAD), the declination and Inclination results of discrete samples (markers) and shipboard u-channel analysis as well as the final magnetostratigraphic interpretation.

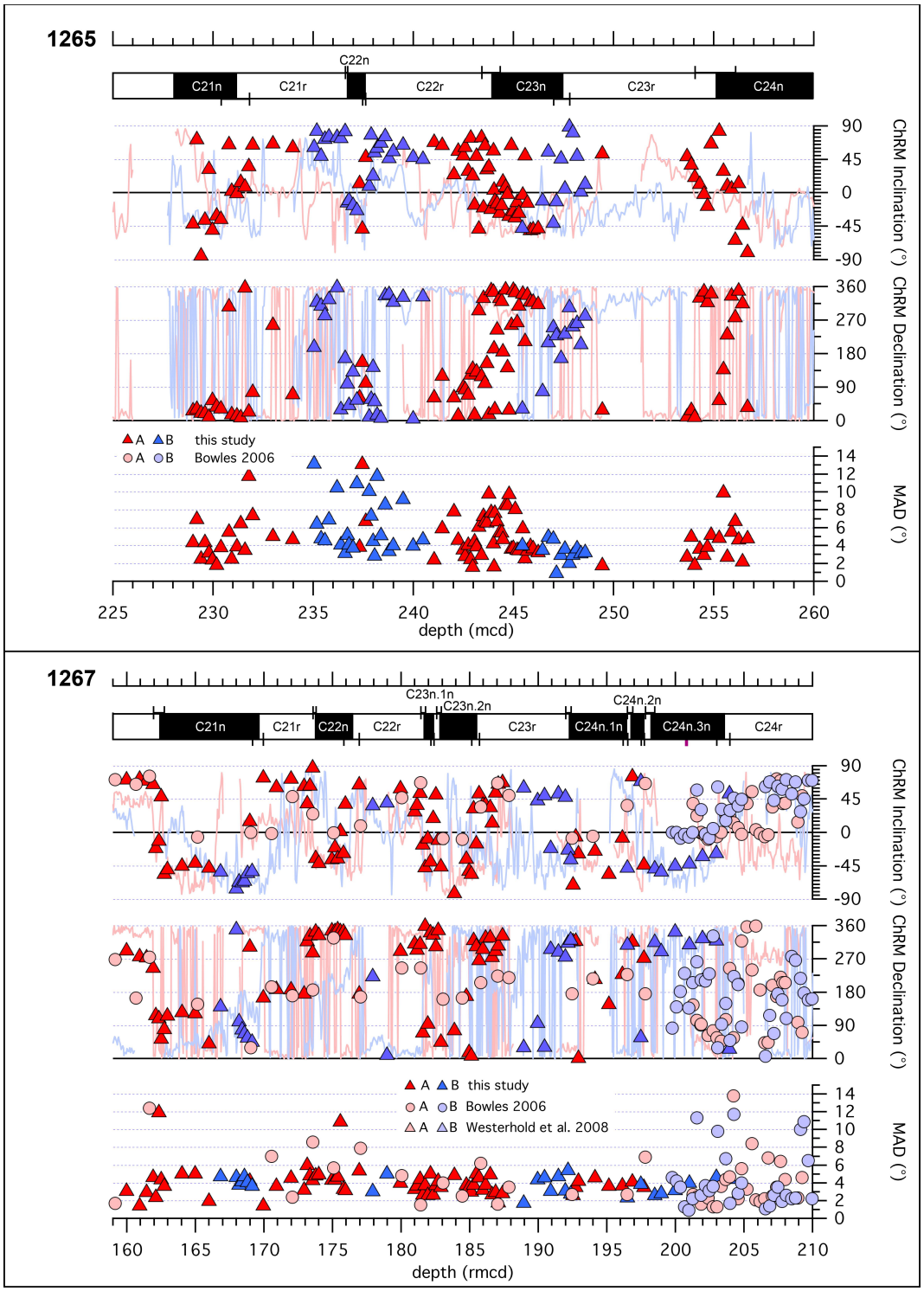

Figure S4b Overview of characteristic remanent magnetization results and data from Leg 208 Sites 1265 and 1267 versus depth. Given for each Site are the maximum angular deviation (MAD), the declination and Inclination results of discrete samples (markers) and shipboard u-channel analysis as well as the final magnetostratigraphic interpretation.

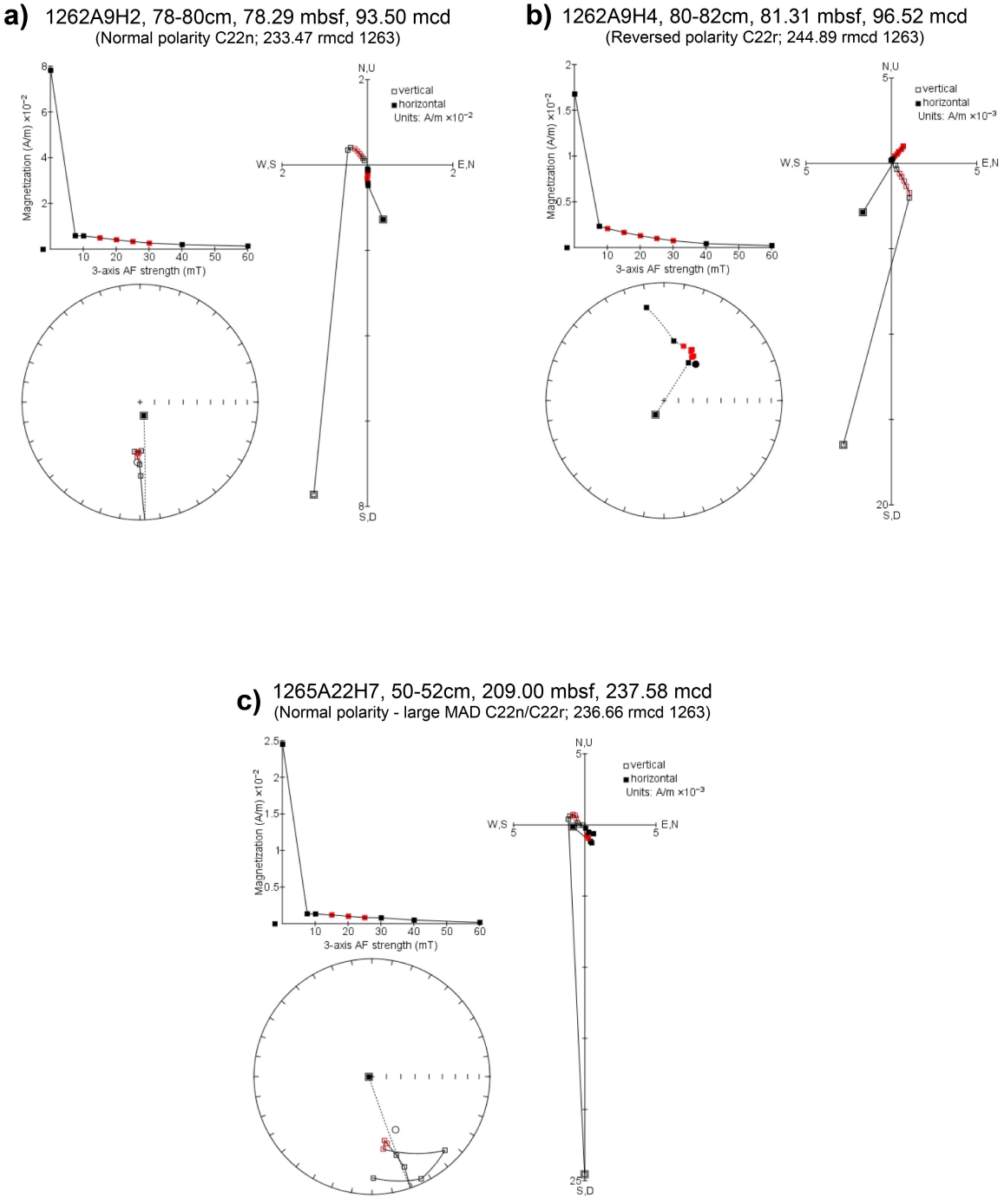

Figure S5 Showcase Zijderveld plots (Z plots) for samples from C22n 1262A9H2, 78-80cm (a); C22r 1262A9H4, 80-82 cm (b); C22n/C22r with large MAD 1265A22H7, 50-52 cm (d). Zijderveld plots were realized with PuffinPlot software (Lurcock and Wilson, 2012). For discussion see text.

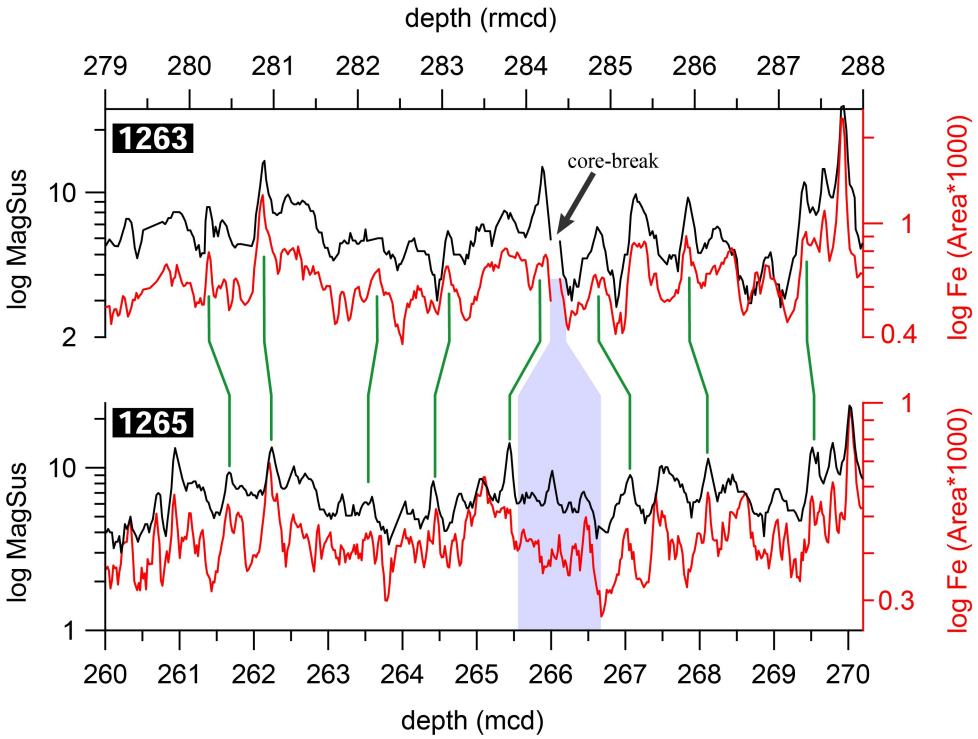

Figure S6 Correlation between ODP Site 1263 and 1265 reveals a gap of three sedimentary cycles in 1263. XRF core scanning Fe intensity (red) and shipboard magnetic susceptibility (black) data are plotted on the respective composite depth. Green lines indicate correlation between sites based on the distinct patterns in the data. Due to very small overlap of cores the splice jump between 1263C9H7-CC and 1263A28H1-1 at 284.34 rmcd was not unambiguous. The correlation shows that in that core break almost a meter of sediment is missing in 1263, clearly present in sediments from 1265.

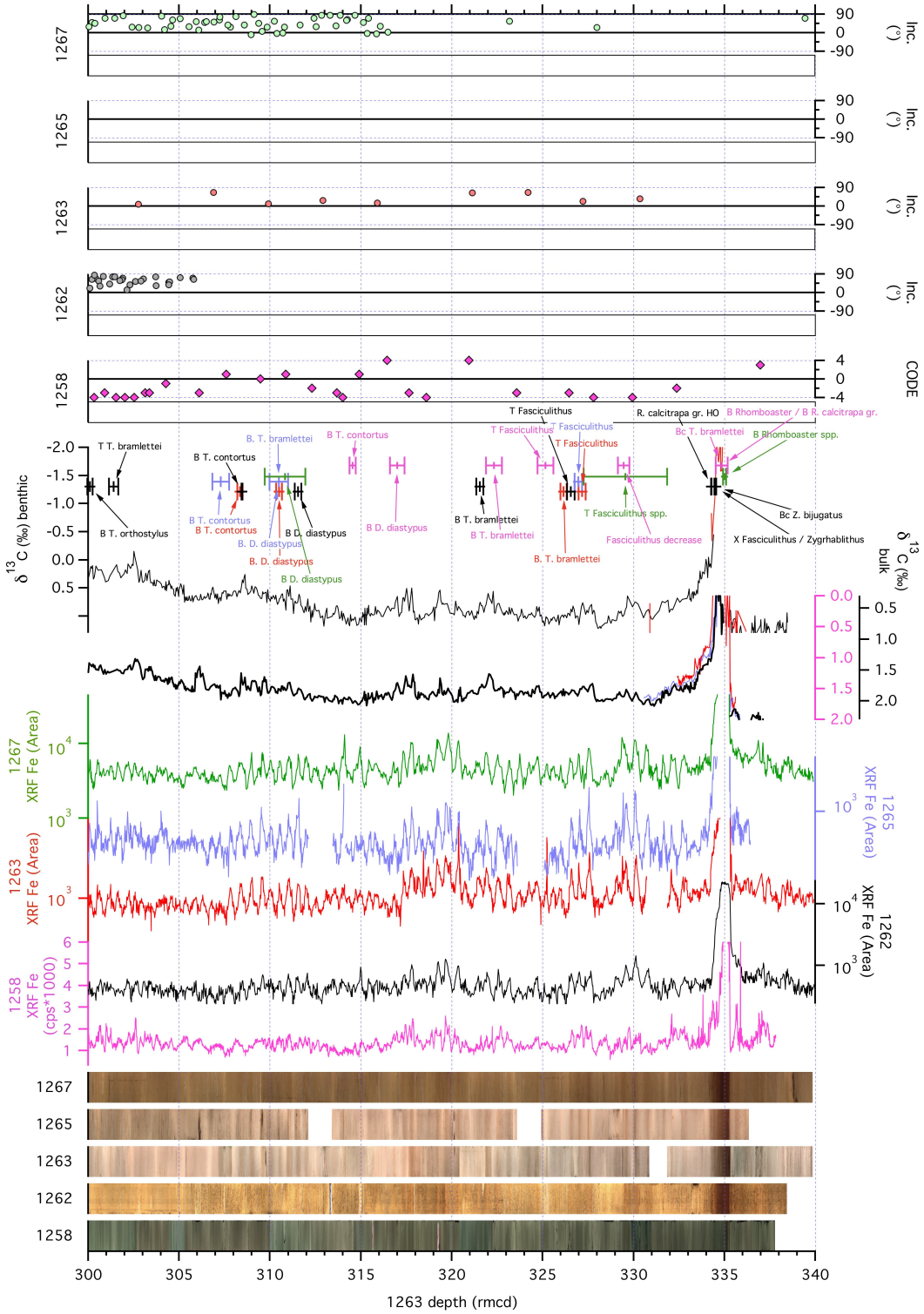

Figure S7 Overview of bio- and magnetostratigraphic data, XRF core scanning Fe intensity data and core images from ODP Site 1258, 1262, 1263, 1265 and 1267 from 300-340 revised meters composite depth of Site 1263. Upper five panels show the inclination from charateristic remanent magnetization investigations from this and previous studies. The position of calcareous nannofossil events including the depth error is plotted for all sites followed by the compiled benthic and bulk $\delta^{13}C$ data and XRF core scanning Fe intensities. For detailed source of data see manuscript text. Purple – 1258, Black and Grey – 1262; Red – 1263; Blue – 1265, Green – 1267.

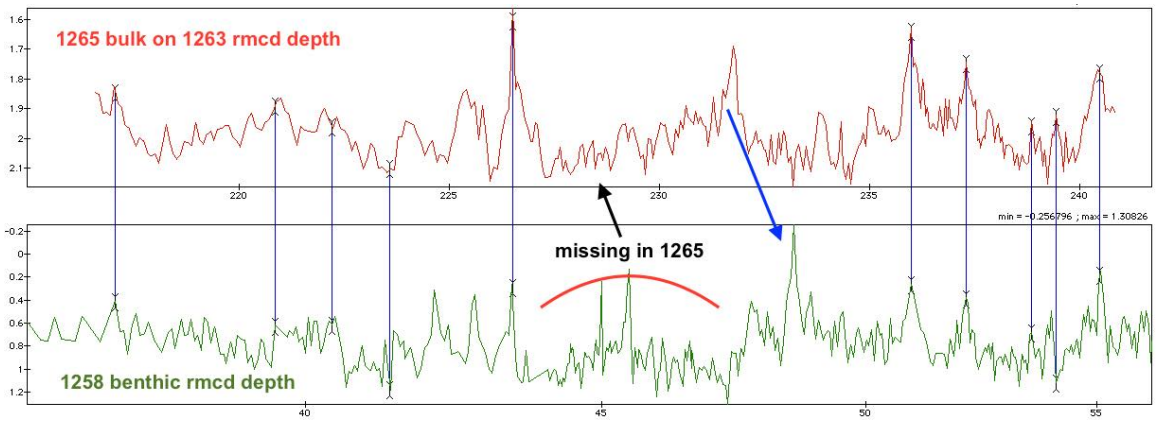

Figure S8 Correlation of bulk carbon isotope data of Site 1265 (red, this study) and benthic carbon isotope data of Site 1258 (green, Sexton et al. 2011) to show the missing or condensed interval in the Leg 208 sedimentary sequence. The missing interval highlighted by the red curve spans roughly one 405-kyr cycle. Blue lines mark the correlation ties between 1258 and 1263 (1265 is plotted on the rmcd 1263), the blue arrow indicates a possible additional correlation tie.

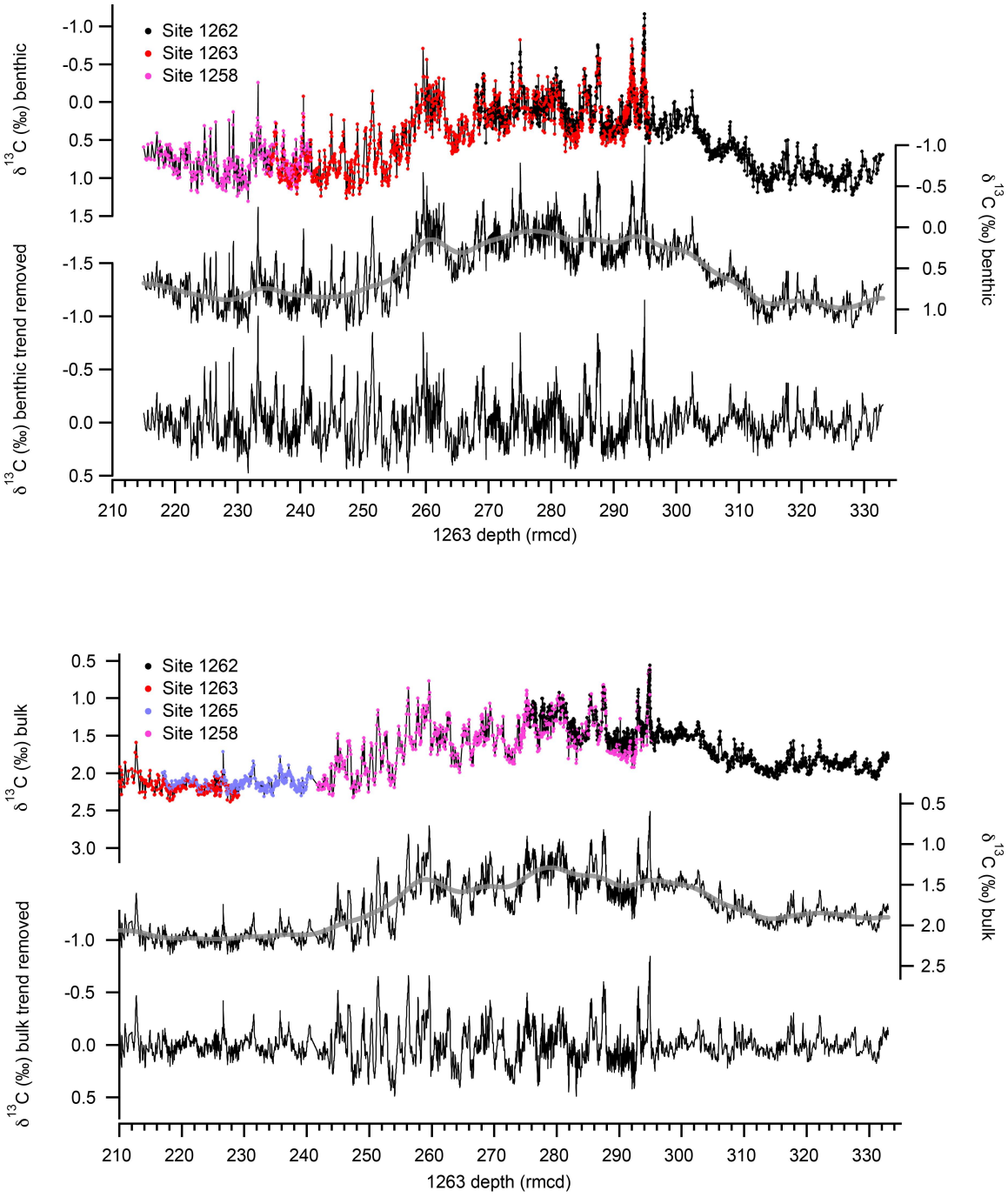

Figure S9 Plot to illustrate the detrending procedure applied to the bulk (lower panel) and benthic (upper panel) stable carbon isotope data compilations. First, all available carbon isotope data have been compiled from multiple sites based on the correlation to Site 1263; Second, a long-term average (thick grey) was defined graphically to avoid removing he apparent 405-kyr cycle; Third, the compiled data were detrended by the long-term average. Source for isotope data is given in the text.

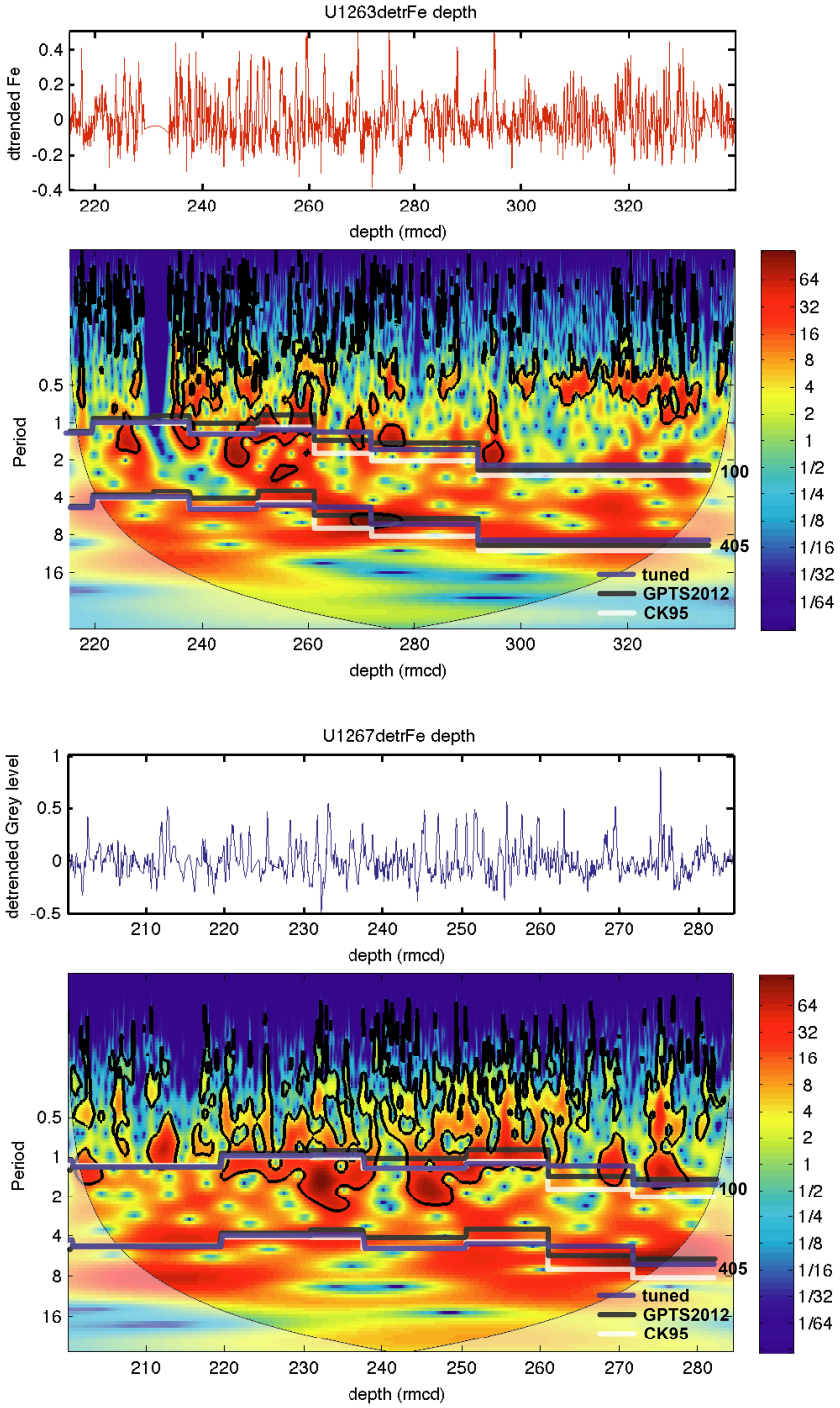

Figure S10a Evolutive wavelet spectra for detrended XRF Fe (1263 – upper panel, 1267 – lower panel) data versus depth. The shaded contours in the evolutionary wavelet power spectra are normalized linear variances, with blue representing low spectral power and red representing high spectral power. The black contour lines enclose regions with more than 95 % confidence. Shaded regions on either end indicate the cone of influence where edge effects become important. Distinct bands that run across the spectra indicate the dominance of Milankovitch frequencies. The top and bottom thick lines are the projected 100 and 405 kyr cycle path using CK95 and GPTS2012 magnetostratigraohic ages, respectively. Also given is the cycle path after orbital tuning for comparison.

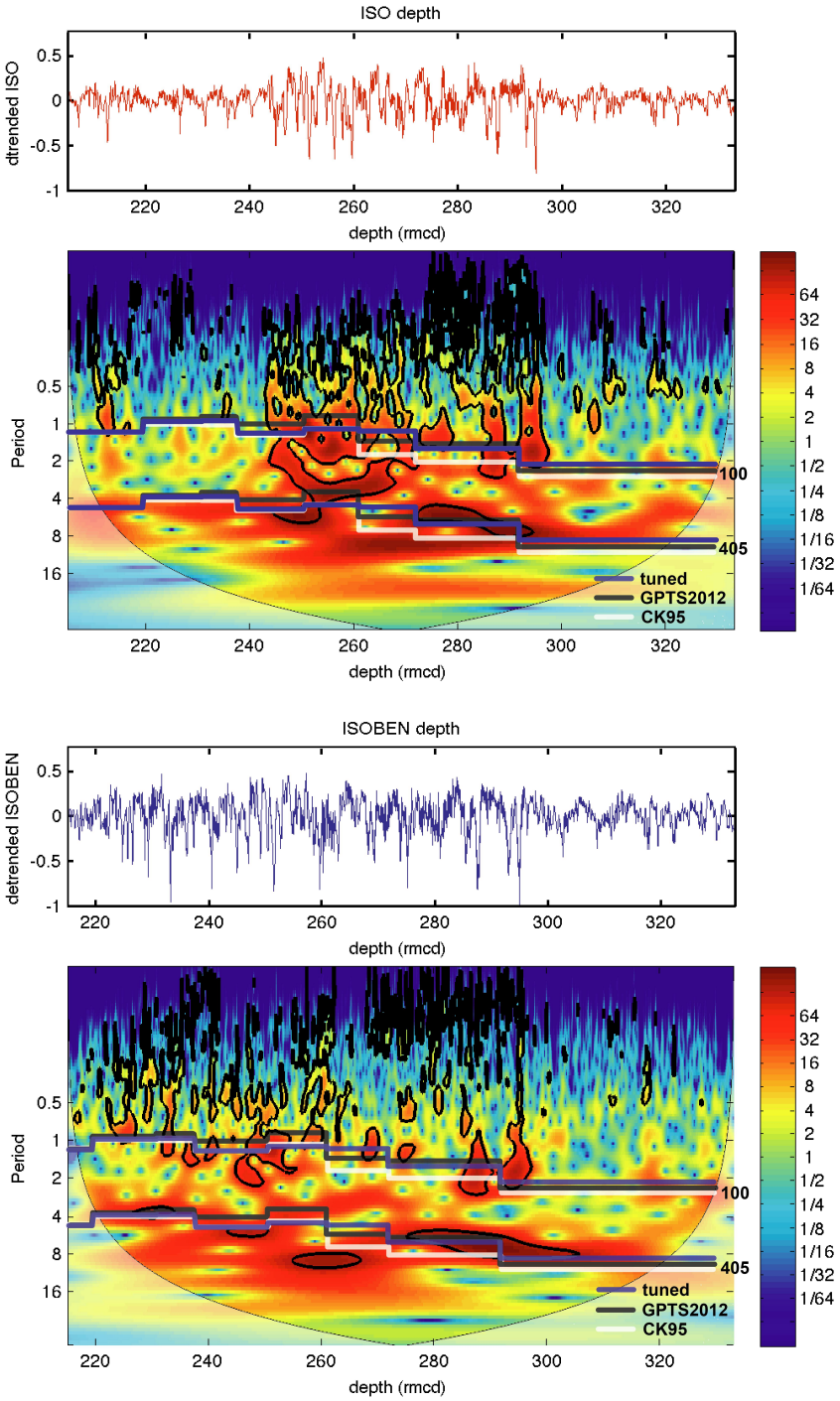

Figure S10b Evolutive wavelet spectra for detrended bulk (ISO, upper panel) and benthic (ISOBEN, lower panel) versus depth. For details see legend of Fig. S10a.

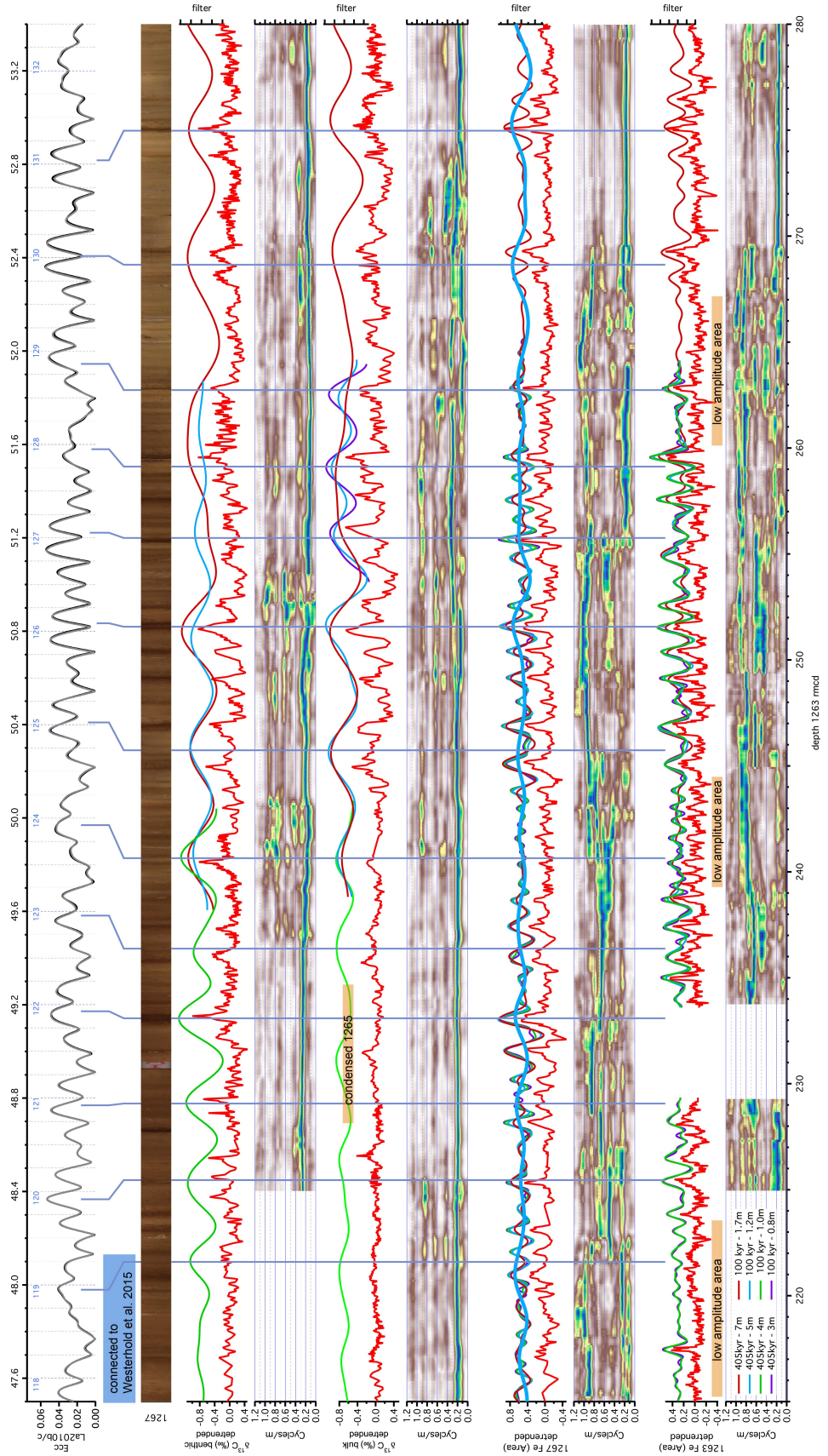

Figure S11 Time series analysis to identify the 100-kyr and 405-kyr eccentricity components in detrended XRF Fe intensity and carbon isotope data for the interval from ETM-2 (275 rmcd 1263) to 220 rmcd 1263 (Chron C21n). Lower two panels show evolutive power spectra for XRF Fe intensities from Site 1262 and 1267 as well as the Gaussian (30% bandwidth) filtered 100- and 405-kyr components as depicted from the power spectra. Upper two evolutive power spectra are from the bulk and benthic carbon isotope compilation. Above the Site 1267 composite core image the La2010b and La2010c orbital solution for eccentricity (Laskar et al. 2011) and the respective 405-kyr number counted from today back in time are shown. The filtered periods are color coded and areas of low amplitude in the data are highlighted. Connected to the stable part of the Eocene cyclostratigraphic framework (see Westerhold et sl. 2015) the blue lines mark the first order tie points for the Ypresian 405-kyr cyclostratigraphy.

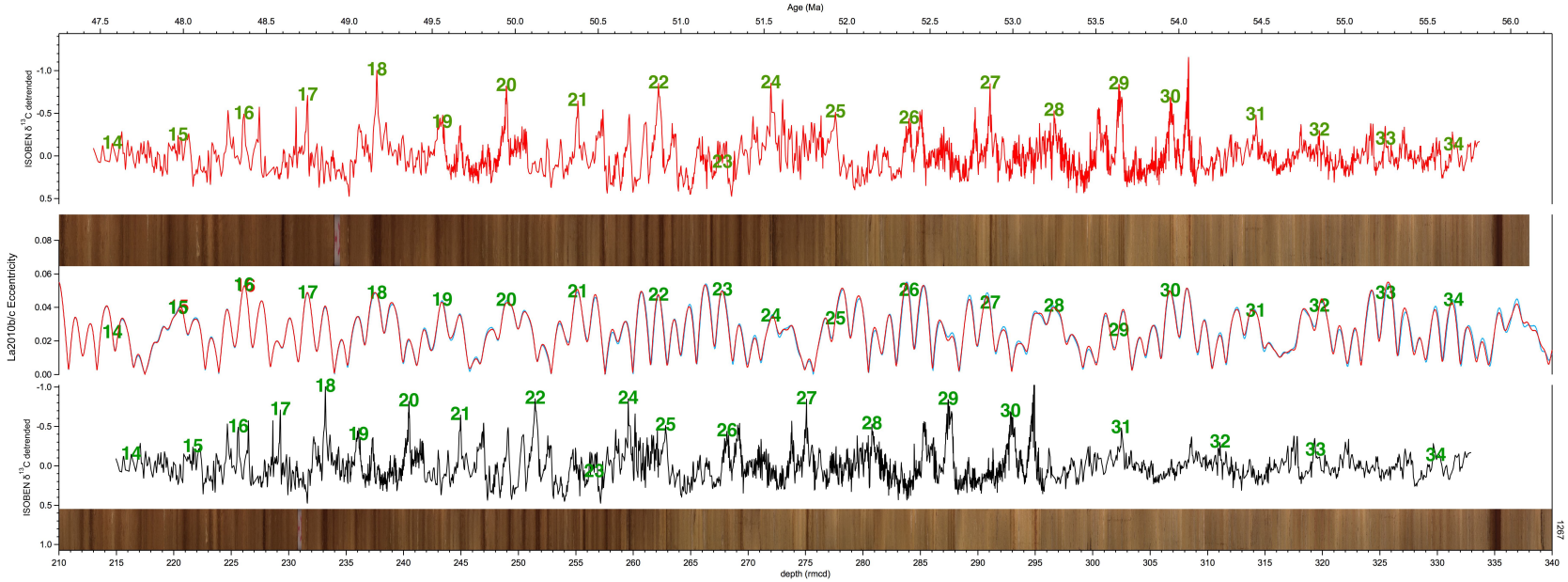

Figure S12 405-kyr tuning of the benthic carbon isotope compilation to La2010b/c from 47.5-56 Ma. Core image of Site 1267 and the benthic carbon isotope compilation on rmcd 1263 in lower panel, La2010b and La2010c orbital solution for eccentricity in the middle panel, and Site 1267 core image and the benthic carbon isotope compilation versus age in the upper panel. The green numbers mark the 405-kyr tie-points as in table S46.

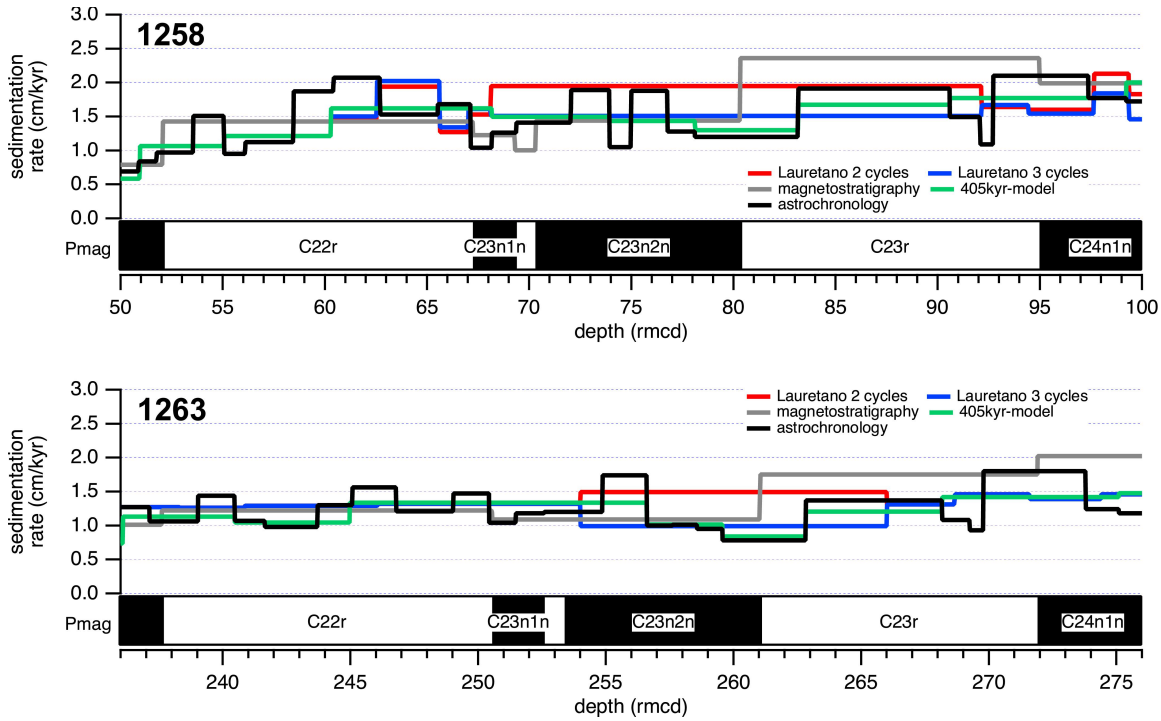

Figure S13 Sedimentation rates for Site 1258 and 1263 applying different age models versus depth and magnetostratigraphy in the interval from Chron C22r to C24n.1n. Red and blue lines are based on the Lauretano et al., (2016) 2 or 3 cycles model, the green line is from the 405-kyr model proposed in this study, the grey line uses the combined magnetostratigraphy developed here with CK95 ages, and the black line is the result of the detailed final astronomical age model from this study. The Lauretano et al., (2016) age models assume no change in sedimentation rates in C23n and C23r. In contrast the magnetostratigraphic model indicates a change in sedimentation rate at both site round the C23n.2n/C23r reversal. See text for discussion.

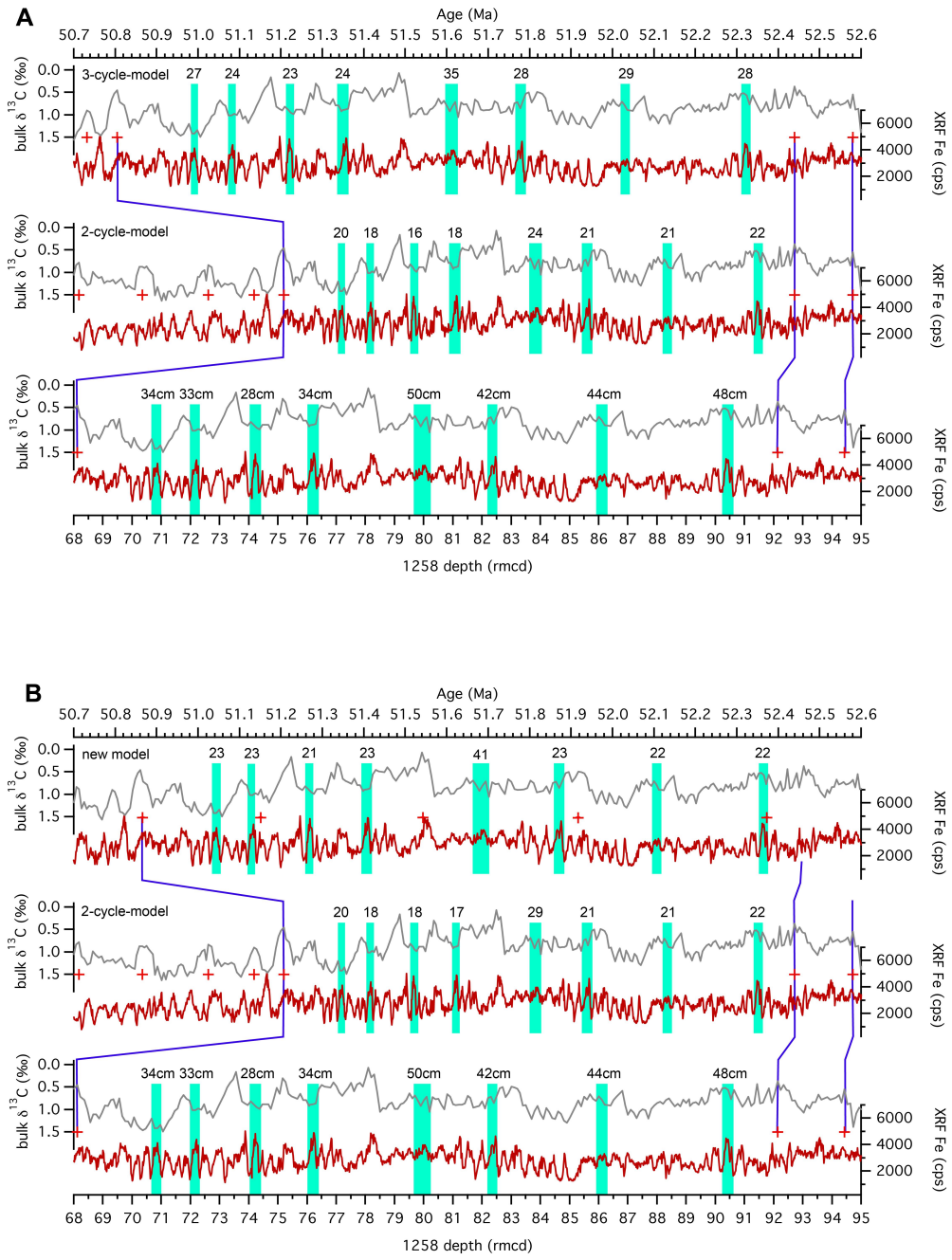

Figure S14 Effect of the 2 and 3 cycle 405-kyr model of Lauretano et al., (2016) (**A**) and the new 405-kyr cycle model developed in this study (**B**) on ODP Site 1258 XRF Fe intensity data (red, Westerhold and Röhl, 2009) and the benthic carbon isotope compilation (grey). In both figure parts the data are plotted versus rmcd depth to illustrate the cycle thicknesses, then the data are plotted versus the Lauretano et al., (2016) 2-cycle-model (the preferred age model in that paper). Eight cycle thickness are highlighted by turquoise bars and the respective thickness in the sediment. The same cycles are then marked in the various age models with the resulting duration for the cycles. The red crossed show the age tie points of each model. The blue lines mark the common age tie points of all models to remind that the Lauretano et al., (2016) age model do not provide tie points between 68 and 92 rmcd in 1258. Assuming most of the cycles are related to precession figure A shows that the 3-cycle-model stretched the cycles too much leading to unrealistically long precession cycles. Figure B suggests that the new 405-kyr model developed here gives remarkably consistent cycles durations for precession cycles and even reveals that the long 50 cm cycles actually are 41-kyr obliquity cycles. For details see the main text.